Journal of Materials Chemistry A

Accepted Manuscript

ROYAL SOCIETY OF CHEMISTRY

www.rsc.org/materialsA

Journal Name Journal of Materials Chemistry A Dynamic Article Links ►

Cite this: DOI: 10.1039/c0xx00000x

www.rsc.org/xxxxxx

ARTICLE TYPE

Phase transformation and cycling characteristic of Ce_2Ni_7-type single-phase $La_{0.78}Mg_{0.22}Ni_{3.45}$ metal hydride alloy

Lu Zhang,[a,b] Yuan Li,[a,b] Xin Zhao,[c] Jingjing Liu,[a,b] Dandan Ke,[a,b] Wenkai Du,[a,b] Shuqin Yang[a,b] and Shumin Han*[a,b]

Received (in XXX, XXX) Xth XXXXXXXXX 20XX, Accepted Xth XXXXXXXXX 20XX
DOI: 10.1039/b000000x

The Ce_2Ni_7-type single-phase $La_{0.78}Mg_{0.22}Ni_{3.45}$ alloy has been prepared by zoning annealing the as-cast sample. It is found that at temperature under 890 ˚C, non-super-stacking $CaCu_5$- and $MgCu_4Sn$-type phases disappear and super-stacking Ce_5Co_{19}-, Gd_2Co_7- and Ce_2Ni_7-type phases remain. The Ce_5Co_{19}-type phase can totally transform to the Ce_2Ni_7-type phase via a peritectic reaction at temperature of 890–900 ˚C. At temperature of 900–950 ˚C, the Gd_2Co_7-type phase melts and decomposes to the Ce_5Co_{19}-type phase, and the newly formed Ce_5Co_{19}-type phase subsequently reacts to form the Ce_2Ni_7-type phase. The Ce_2Ni_7-type single phase stays stable at even higher temperature of 950–975 ˚C. The single-phase alloy shows superior discharge capacity, close to 394 mAh g^{-1}, and high electrochemical cycling stability, which can achieve 413 cycles as its discharge capacity reduces to 60% of the maximum value. We found the capacity attenuation of the single-phase alloy is mainly due to the loss of active material at the alloy surface caused by oxidization of La and Mg, and the pulverization of the alloy is not severe with 100 charge/discharge cycles. Crystal structure of the single-phase alloy can preserve well. Oxidation of La occurs prior to that of Mg. La hydroxide grows from nano-structured needles to larger-scaled rods then to unformed lamellar hydroxide, whereas the precipitation of Mg forms as irregular lamellae inlaid with hexagonal flakes.

1. Introduction

Rechargeable nickel metal hydride battery (Ni/MH battery) is expected to take a leading role in battery-powered/assisted vehicle and personal portable electronics applications due to its high capacity, environmental friendly and safety characteristics.[1–3] Recently, new groups of super-stacking A_2B_7-type La–Mg–Ni-based negative alloys have become the optimal candidate to replace currently used AB_5-type misch-metal based alloys, due to their higher capacity and better high-rate dischargeability (HRD).[4,5] However, poor cycling stability remains as the major drawback for A_2B_7-type La–Mg–Ni-based alloys.

In order to improve the cycling stability of A_2B_7-type La–Mg–Ni-based alloys, it is essential to get a good understanding of the cause of their discharge capacity degradation. There are some studies reported in the literature. For example, Liu et al. found that the fast capacity degradation of $La_{0.7}Mg_{0.3}Ni_{3.4}Mn_{0.1}$ alloy during cycling is attributed to two main factors, the intense pulverization and oxidation/corrosion of the active components.[6] Further studies on the capacity degradation mechanism of $La_{0.7}Mg_{0.3}Ni_{3.4-x}Co_xMn_{0.1}$ (x = 0, 0.75, 1.3) alloys show the mechanism is composed of three consequent stages: 1) the pulverization and Mg oxidation stage, 2) the Mg and La oxidation stage, and 3) the oxidation and pulverization stage.[7] Based on previous studies, pulverization of the alloy particles, which is caused by lattice expansion/contraction due to hydrogen absorption/desorption, and oxidation/corrosion of the active materials induced by the interaction between the alloy surface and electrolyte during electrochemical cycling are believed to be the causes of the discharge capacity degradation.[8] Furthermore, from a structure perspective, recent studies on ternary La–Mg–Ni alloys show that their poor cycling stabilities can be attributed to the formation of multiphase structures of those alloys.[9] Large amounts of lattice strain among the phase boundaries and changes in desynchronized cell volume due to expansion/contraction during hydrogen absorption/desorption processes can both lead to aggravated pulverization of the multiphase alloys.[10,11] As a result, pulverization leads to formation of more active surfaces from the alloy, causing severe oxidation/corrosion of the active material of the multiphase alloys.[12] For multiphase alloys, the pulverization and oxidation/corrosion processes of one phase are interconnected with other phases. This makes the determination of the pulverization and oxidation/corrosion processes for one specific phase in the capacity degradation process difficult.

Therefore, in order to understand the discharge capacity degradation of A_2B_7-type alloys, it is important to accurately study the capacity degradation process of one single-phase $(La,Mg)_2Ni_7$ alloy.

However, preparation of single-phase $(La,Mg)_2Ni_7$ alloys is difficult due to their similar composition and narrow temperature range between each super-stacking phase.[13] Since Denys et al. accidentally obtained the Ce_2Ni_7-type single-phase $La_{1.5}Mg_{0.5}Ni_7$ alloy by stepwise sintering method in 2007,[14] only a few Ce_2Ni_7-type single-phase $(La,Mg)_2Ni_7$ alloys have been reported in recent years.[15–17] Guzik et al. prepared $La_{1.64}Mg_{0.36}Ni_7$ and $La_{1.63}Mg_{0.37}Ni_7$ alloys by sintering La–Ni intermetallic and Mg powder and studied their hydrogen site configuration.[16] Recently, we reported preparation of a Ce_2Ni_7-type single-phase $La_{1.6}Mg_{0.4}Ni_7$ alloy via the method of annealing the induction melting and studied its phase decomposition characteristic.[17] Although some Ce_2Ni_7-type single-phase $(La,Mg)_2Ni_7$ alloys have been obtained in various methods, detailed study on the formation mechanism of those Ce_2Ni_7-type single-phase alloys during the preparation process is still missing.

In this paper, based on our previous studies, we adopted zoning annealing treatment method to prepare a Ce_2Ni_7-type single-phase $La_{0.78}Mg_{0.22}Ni_{3.45}$ alloy. The formation mechanism of the Ce_2Ni_7-type single-phase is elucidated, and its hydrogen storage characteristics and electrochemical properties are studied. More importantly, the mechanism of discharge capacity degradation of the single-phase alloy during cycling is discussed in detail.

2. Experimental Section

2.1. Preparation of the alloy

The as-cast $La_{0.78}Mg_{0.22}Ni_{3.45}$ alloy was firstly designed according to the evaporation of Mg during annealing treatment to obtain the previous $La_{1.6}Mg_{0.4}Ni_7$ alloy. The $La_{0.78}Mg_{0.22}Ni_{3.45}$ alloy was prepared by induction melting the constituent metals, including La, Mg and Ni, with a purity of 99.5%. A La–Ni metal block was first heated to a molten state, and a Mg metal piece was placed into the smelting furnace after temperature dropping to 1600 ˚C while stirring the mixture quickly and vigorously, followed by casting. The resulting blocky as-cast alloy (~10 g) was first wrapped in a nickel foil, placed in a furnace that is kept at an annealing temperature for 12 h (heating rate 4 ˚C min^{-1} below 600 ˚C and 1 ˚C min^{-1} above 600 ˚C) under 0.04 MPa argon atmosphere, and then quenched to room temperature in the furnace. In this study, alloy samples were annealed at a range of annealing temperatures, including 850, 890, 900, 910, 925, 935, 940, 945, 950, 960 and 975 ˚C. A slight excess of Mg was used to compensate for the excess evaporation of Mg during the annealing procedure. The chemical analysis of the alloys was performed using inductively coupled plasma (ICP) analyzers.

2.2. Structure and morphology analysis

The alloys were crushed mechanically into particles (< 400 mesh) for X-ray diffraction (XRD) measurements using a Rigaku D/Max-2500/PC X-ray diffractometer (Cu Kα radiation). The XRD data were collected over a range of 2θ from 10 to 80° with a step of 1° min^{-1} increment and analyzed by the Rietveld method using RIETICA software.[18] Morphology of the alloys was characterized by S-4800 scanning electron microscopy (SEM) and their phase composition was studied by energy dispersive spectrometer (EDS). TEM analysis was performed on JEM-2010 with energy-dispersive X-ray (EDX) operating at 20.0 kV to determine the chemical composition of the samples. X-ray photoelectron spectrometry (XPS) analysis was performed on an ESCALABMKLL X-ray photoelectron spectrometer with monochromatic Al Kα radiation.

2.3. Hydrogen absorption and desorption measurements

Pressure-composition-temperature (PCT) characteristic for each sample was measured using Sieverts' method at 25, 50 and 75 ˚C. Prior to taking PCT measurements, each sample was fully activated by repeatedly hydriding-dehydriding at 50 ˚C for four times. During each activating hydriding-dehydriding cycle, samples were hydrided under a hydrogen pressure of 2 MPa for 1 h and then dehydrided against a backpressure of 0.001 MPa for 1 h.

2.4. Electrode preparation and electrochemical measurements

To prepare the electrode used for half cell electrochemical study, each ingot was first ground mechanically into powder between 200–400 meshes, and the powder (0.15 g) was mixed with nickel powder (0.75 g) to cold press into a pellet of 10 mm under 15 MPa. Electrochemical measurements of the small-sized electrode were measured in an electrochemical cell with $Ni(OH)_2$ sintered electrode as the positive electrode and 6 M KOH solution as the electrolyte. The system was charged at a current density of 72 mA g^{-1} for 8 h (the over-charged ratio approximately 50%) and then discharged at a current density of 72 mA g^{-1} for activation, followed by charging at 360 mA g^{-1} for 1.6 h then discharging at 72 mA g^{-1} for cycling stability measurement with a cut-off potential of 1.0 V. For high rate dischargeability (HRD) measurement, the discharging current density was 1440 mA g^{-1}. Linear polarization was performed by scanning the potential from –5 to +5 mV versus the open circuit voltage at a rate of 5 mV min^{-1}. For the potentiostatic discharge experiment, the electrode in its fully charged state was polarized with +500 mV (vs. the open circuit voltage) steps for 3600 s.

To prepare the cycling samples for XPS, XRD, SEM and TEM measurements, the ingot powder of ca. 0.4 g (neither binder nor Ni powder was added) was directly pressed into a pellet that is then wrapped into a nickel foam, and measured in the half cell configuration. The system was charged at a current density of 55 mA g^{-1} for 10 h and then discharged at a current density of 72 mA g^{-1} until a cut-off voltage of 1.0 V was reached. The cycling samples of 2, 10, 20, 40, 70, 100, 125, 150, 180, 200 and 250 charge-discharge cycles were first collected, then washed with deionized water for 3 times, and dried under Ar protection.

3. Results and discussions

The alloy prepared in this study has a design composition of $La_{0.78}Mg_{0.22}Ni_{3.45}$. The finial ICP results in atomic mass percentage of the ingots before and after annealing (at 890, 900, 925, 935, 945, 950 and 975 ˚C for 12 h) are listed in Table 1. The compositions of the alloys are close to the design value except for a small amount of over-compensating Mg. The final B/A ratios of the annealed alloys are close to the target value (3.45), except for

the as-cast sample and the samples annealed at higher temperatures, which are slightly lower (3.39) and higher (3.49), respectively.

Table 1 Design compositions and ICP results in wt.%

	La	Mg	Ni	B/A
Design	34.32	1.67	64.01	3.45
As-cast	34.60	1.72	63.68	3.39
895 ˚C	34.41	1.69	63.90	3.43
900 ˚C	34.34	1.72	63.94	3.43
925 ˚C	34.26	1.74	64.00	3.43
935 ˚C	34.82	1.56	63.62	3.44
945 ˚C	34.13	1.71	64.16	3.46
950 ˚C	34.40	1.62	63.98	3.47
975 ˚C	34.55	1.51	63.91	3.49

3.1. Structure analysis

The XRD patterns in the 2θ range of 18–40° of the as-cast sample and the annealed samples at 890, 900, 925, 935, 945, 950 and 975 ˚C for 12 h are shown in Fig. 1 (Additional X-ray diagrams are available in the Supplementary Information Fig. S1). As shown in Fig. 1a, the as-cast alloy exhibits five structure phases: 1) the $CaCu_5$-type $LaNi_5$, 2) the Ce_5Co_{19}-type $(La,Mg)_5Ni_{19}$, 3) the Ce_2Ni_7-type $(La,Mg)_2Ni_7$, 4) the Gd_2Co_7-type $(La,Mg)_2Ni_7$, and 5) the $MgCu_4Sn$-type $(La,Mg)_2Ni_4$ phases. When annealed at a temperature of 850 ˚C (Fig. S1), the $CaCu_5$-type and the $MgCu_4Sn$-type phases disappear with only other three super-stacking phases left, and this observation remains until the temperature increases to 890 ˚C. The peaks of the Gd_2Co_7-type phase mostly overlap with those of the Ce_2Ni_7-type phase except at 2θ = 31.88 and 33.72°, which can be seen as its characteristic peaks (anneal at 890–925 ˚C). Characteristic peaks for the Ce_5Co_{19}-type phase at 2θ = 31.66 and 33.42° can be observed in the XRD pattern of the samples annealed at 935 and 945 ˚C (Fig. 1b). According to these characteristic peaks, it can be concluded that, as the annealing temperature increases to 900 ˚C, the Ce_5Co_{19}-type phase is absent and the sample consists of the double-phase Ce_2Ni_7-type and the Gd_2Co_7-type structures till the annealing temperature reaches 925 ˚C. Further increase in the annealing temperature to 935 ˚C, the Gd_2Co_7-type phase disappears but the Ce_5Co_{19}-type phase reappears, and the Ce_2Ni_7- and Ce_2Co_{19}-type phases coexist in the temperature range of 935–945 ˚C. Finally, in the annealing temperature range of 950–975 ˚C, the Ce_2Ni_7-type single-phase alloys with the compositions of $La_{0.79}Mg_{0.21}Ni_{3.47}$ (950 ˚C) and $La_{0.8}Mg_{0.2}Ni_{3.49}$ (975 ˚C) are obtained. Fig. 2 shows the Rietveld refinements of the X-ray diffraction data for some annealed alloys, and results in terms of phase abundance and lattice parameters of all alloys are listed in Table 2. For both the as-cast and the annealed alloys, lattice constants a and c of the Ce_2Ni_7-type phase for each alloy remain between 5.0401–5.0416 Å and 24.301–24.321 Å, respectively. The results of XRD and Rietveld refinements indicate that phase transformation occurs during annealing process and the alloy patterns are dominated by the Ce_2Ni_7-type phase. Based on the La–Ni phase diagram[19] and the results of Rietveld refinements, one may deduce that the $CaCu_5$-type and the $MgCu_4Sn$-type phases convert to super-stacking phases via peritectic reactions when annealing at 890 ˚C. Since the masses of the three super-stacking phases all increase, it is impossible to determine which super-stacking phase the $CaCu_5$-type and the $MgCu_4Sn$-type phases convert to. We can only conclude that the $CaCu_5$-type and the $MgCu_4Sn$-type phases can be easily transformed to super-stacking phases via peritectic reactions at lower temperature. As the temperature increases from 890 to 900 ˚C, the Ce_5Co_{19}-type phase has transformed to the Ce_2Ni_7-type phase because the phase abundance of the Ce_2Ni_7-type phase increases from 78.84 to 85.93 wt.% but the phase abundance of the Gd_2Co_7-type phase remains almost unchanged (15.05 to 14.07 wt.%). Therefore, the Ce_2Ni_7-type and the Gd_2Co_7-type phases coexist when the temperature is up to 900 ˚C. As the temperature increases to 925 ˚C, the relative amount of the Ce_2Ni_7-type phase increases from 85.93 to 91.97 wt. %, indicating that the Ce_2Ni_7-type phase is thermodynamically stable at a higher temperature and the Gd_2Co_7-type phase transforms to the Ce_2Ni_7-type phase. However, the Gd_2Co_7-type phase dose not totally transform to the Ce_2Ni_7-type phase with a further increase in temperature. Instead, it transforms to the Ce_5Co_9-type phase in the temperature range of 925–935 ˚C. The abundance of the Ce_5Co_9-type phase gradually

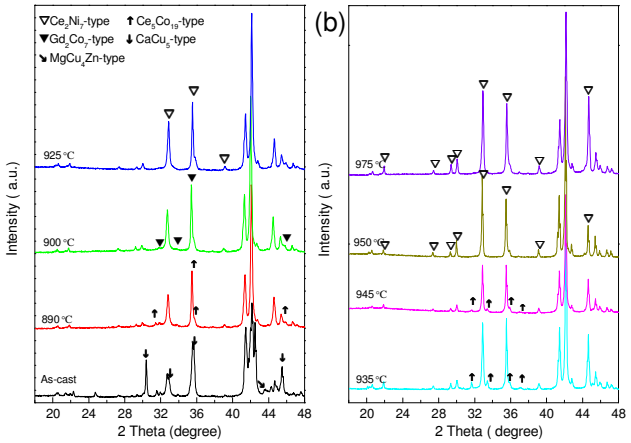

Fig. 1 Evolution of the XRD patterns in the 2θ range of 18–40° for the as-cast alloy and alloys annealed at 890–925 ˚C (a) and 935–975 ˚C (b).

Table 2 Lattice parameters and phase abundances of alloys from XRD and Rietveld analysis

Alloy	Str. type	*a* (Å)	*c* (Å)	Abundance (wt.%)
As-cast	Ce_2Ni_7	5.0401	24.301	58.01
	Gd_2Co_7	5.0411	36.289	10.83
	Ce_5Co_{19}	5.0301	48.182	11.05
	$CaCu_5$	5.0294	4.001	15.06
	$MgCu_4Sn$	7.1652	-	5.05
895 ˚C	Ce_2Ni_7	5.0404	24.313	78.84
	Gd_2Co_7	5.0410	36.312	15.05
	Ce_5Co_{19}	5.0315	48.212	6.11
900 ˚C	Ce_2Ni_7	5.0403	24.317	85.93
	Gd_2Co_7	5.0409	36.301	14.07
925 ˚C	Ce_2Ni_7	5.0406	24.348	91.97
	Gd_2Co_7	5.0411	36.311	8.03
935 ˚C	Ce_2Ni_7	5.0401	24.321	92.75
	Ce_5Co_{19}	5.0275	48.199	7.25
945 ˚C	Ce_2Ni_7	5.0411	24.311	95.30
	Ce_5Co_{19}	5.0274	48.169	4.70
950 ˚C	Ce_2Ni_7	5.0412	24.291	100
975 ˚C	Ce_2Ni_7	5.0416	24.304	100

decreases with increasing temperature until it converts to the single-phase Ce_2Ni_7-type in the range of 945–950 ˚C.

From the above observations, we may deduce that the Ce_2Ni_7-type phase was formed by a peritectic reaction between the Ce_5Co_9-type phase and one liquid phase in the entire process. In the temperature range of 900–925 ˚C, the Gd_2Co_7-type phase first melts and decomposes to the Ce_5Co_{19}-type phase and a liquid phase, and the newly formed Ce_5Co_{19}-type phase subsequently converts to the Ce_2Ni_7-type phase via a peritectic reaction, where the reaction rate of the decomposition of the Gd_2Co_7-type phase is slower than the peritectic reaction. Therefore, no Ce_5Co_9-type phase was detected in this temperature range. As temperature increases from 925 to 935 ˚C, the Gd_2Co_7-type phase has been totally depleted to the Ce_5Co_{19}-type phase, and the Ce_5Co_{19}-type phase may be more stable at this temperature range, which leads to the slow reaction rate. Therefore, the alloys are composed of the Ce_2Ni_7/Ce_5Co_{19} phase structure within 935–945 ˚C, and the Ce_5Co_{19}-type phase continues reacting with the liquid phase by a peritectic reaction to form the Ce_2Ni_7-type phase in a slow reaction rate till 950 ˚C. The phase abundance of the Ce_2Ni_7-type increases with increasing annealing temperature in the entire process, and the Ce_2Ni_7-type single phase ultimately stays stable in a wide temperature range of 950–975 ˚C (as shown in Fig. S1). The alloy's structural transformations with annealing temperature are shown as Table 3.

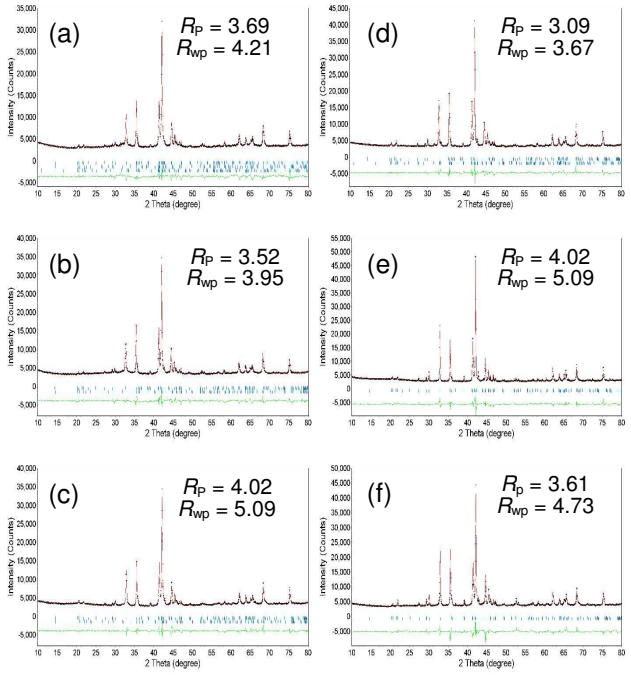

Fig. 2 Rietveld refinement of XRD patterns for the alloy annealed at 890 ˚C (a), 900 ˚C (b), 925 ˚C (c), 945 ˚C (d), 950 ˚C (e) and 975 ˚C (f).

Furthermore, we observe that the minor phases can continuously transform to a main phase (generally speaking, its abundance is more than 50 wt.% for the as-cast alloy) under an appropriate annealing temperature condition. This result has also been reported by Young et al. on the $(Nd,Mg,Zr)(Ni,Al,Co)_{3.74}$ alloy.[8] Unlike the La–Mg–Ni-based alloys, the Nd–Mg–Ni-based alloy still contains some minor phases other than A_2B_7-type phase when annealing at 950 ˚C. This may be attributed to the annealing temperature of 950 ˚C not being high enough for the Nd–Mg–Ni-based alloy due to its higher reaction temperatures as seen in the Nd–Ni phase diagram.[20] Therefore, we can conclude that some single-phase alloys can be prepared by annealing the as-cast alloy under an appropriate annealing condition.

Table 3 Changes in phase composition with annealing temperature of the alloy

Tem. (˚C)	Phase composition	Phase transformation
890	$Ce_2Ni_7/Gd_2Co_7/Ce_5Co_{19}$	
890–900		Ce_5Co_{19} + liquid → Ce_2Ni_7
900	Ce_2Ni_7/Gd_2Co_7	
900–925		$Cd_2Co_7 \rightarrow Ce_5Co_{19}$ + liquid Ce_5Co_{19} + liquid → Ce_2Ni_7
925	Ce_2Ni_7/Gd_2Co_7	
925–935		$Cd_2Co_7 \rightarrow Ce_5Co_{19}$ + liquid
935–945	Ce_2Ni_7/Ce_5Co_{19}	
945–950		Ce_5Co_{19} + liquid → Ce_2Ni_7
950–975	Ce_2Ni_7	

The microstructures of the annealed alloys are studied by SEM and presented in Fig. 3. Compositions in several areas (alphabetized in the micrographs) are analyzed by EDS. As shown in Fig. 3a, phases with the brightest (area A_1) and darkest (area B) contrasts are A_2B_7-type with a composition of $La_{0.85}Mg_{0.14}Ni_{3.48}$ and A_5B_9-type with a composition of $La_{0.82}Mg_{0.18}Ni_{4.13}$, respectively. The mid-contrast (area A_2) is also an A_2B_7-type structure, but its Mg content is higher than that of area A_1 by 0.1. Similarly, in Fig. 3b, content of Mg in area A_2 (0.25) is also higher than that in area A_1 (0.20), but B/A ratios of the two areas are both 3.5, indicating that they are both A_2B_7-type phases. We failed to differentiate the Ce_2Ni_7-type from the Gd_2Co_7-type structure for these two areas by SEM analysis; therefore, TEM analysis is performed and will be further discussed in the later session of this paper. From the results above, it is evident that Mg can easily pass the phase boundaries of similar structure and forms A_2B_7-type phases with different solid solution of Mg in the annealing process. As a result, different contrast areas are observed in the images, in which the Mg-rich region is darker than the Mg-poor region due to the tendency of being corroded under a corrodent $FeCl_3$ environment, resulting in a lower plane for Mg-rich region. Parts c and d of Fig. 3 are samples annealed at 935 and 945 ˚C, respectively. The main Ce_2Ni_7-type phase is the brighter contrast area (area A) and the darker area corresponds to the Ce_5Co_{19}-type phase (area B), according to XRD and Rietveld refinement results. Moreover, the Ce_2Ni_7-type main phase exhibits a waving shape and the Ce_5Co_{19}-type phase is embedded in that main phase. It suggests that the elements in the Ce_5Co_{19}-type phase have homogenized during the annealing process and the homogenization begins at the boundaries of the two phases then continues to the center of the Ce_5Co_{19}-type phase, thereby forming a mosaic shape for the Ce_5Co_{19}-type phase. This also manifests the occurrence of the peritectic reaction of the Ce_5Co_{19}-type phase into the Ce_2Ni_7-type main phase. Parts e and f of Fig. 3 show the homogenous compositions of $La_{0.80}Mg_{0.20}Ni_{3.46}$ and $La_{0.80}Mg_{0.20}Ni_{3.50}$, respectively. Similarly to the ICP results, this indicates that the Ce_5Co_{19}-type phase is fully homogenized by the Ce_2Ni_7-type, and

the Ce_2Ni_7-type phase stays stable within the temperature range of 950–975 ˚C.

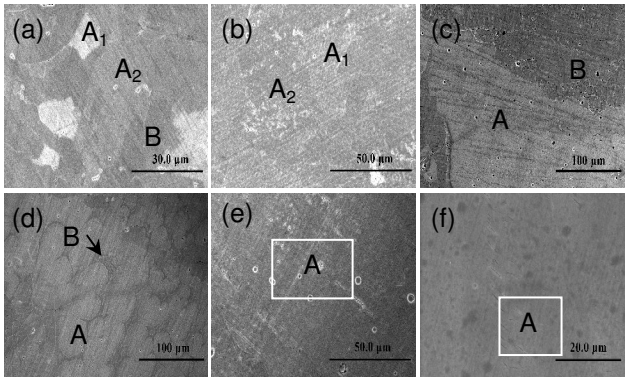

Fig. 3 SEM analysis of the alloy annealed at 890 ˚C (a), 900 ˚C (b), 935 ˚C (c), 945 ˚C (d), 950 ˚C (e) and 975 ˚C (f).

TEM images of the sample annealed at 900 ˚C are shown in Fig. 4, to reveal the specific microstructures of the Ce_2Ni_7- or the Gd_2Co_7-type in the A_2B_7-type phase. Fig. 4a,b is the low magnification bright field TEM images of the Ce_2Ni_7-type grain and the Cd_2Co_7-type grain, and their structures are identified by selected area electron diffraction (SAED) as shown in Fig. 4c,d, respectively. SAED analysis of these two grains is performed in three directions in order to better distinguish their structures. The results show that the bigger/thicker grain in Fig. 4a is the Ce_2Ni_7-type structure and the smaller/thinner one in Fig. 4b is the Gd_2Co_7-type structure. Accordingly, SAED patterns along the zone-axis [001] for the Ce_2Ni_7-type structure and along the zone-axis [331] for the Gd_2Co_7-type structure are shown in Fig. 4c,d, respectively. Based on the TEM analysis, it can be deduced that grain boundary between the Ce_2Ni_7- and the Gd_2Co_7-type structures is unstable, which can be easily separated under external force during sample preparation. Meanwhile, the few Gd_2Co_7-type grains may distribute in a layer form among the Ce_2Ni_7-type grains, leading to a thin film-like morphology of the Gd_2Co_7-type grains after separation, thereby appearing of the kikuchi line in the image.

3.2. Gaseous phase study

The gaseous phase hydrogen storage properties of the annealed alloys were studied by PCT measured at 25, 50, and 75 ˚C. The PCT results are summarized in Table 4. The absorption /desorption isotherms, Van't Hoff plots and hydrogen absorption curves for the alloys annealed at 900, 935, and 950 ˚C, corresponding to three groups of alloys with different phase compositions (Ce_2Ni_7-type main phase with Gd_2Co_7-type minor phase, Ce_2Ni_7-type main phase with Ce_5Co_{19}-type minor phase, and Ce_2Ni_7-type single phase), are shown in Fig. 5a–c,d,e, respectively.

The single-phase alloys (annealed at 950–975 ˚C) show the highest maximum hydrogen storage capacities and reversible hydrogen storage capacities among these three groups of alloys, followed by the double-phase alloys with minor Cd_2Co_7-type phase. The alloys with minor Ce_5Co_{19}-type phase show the lowest maximum hydrogen storage capacities and reversible hydrogen storage capacities among these three. The hydrogen storage capacities of the alloys correlate well with their A_2B_7-type phase abundance, indicating that gas-solid hydrogen storage capacity of the A_2B_7-type (Ce_2Ni_7-type and Cd_2Co_7-type) phase is superior, especially for the Ce_2Ni_7-type single-phase alloys. The equilibrium plateau pressures of the alloys, defined as the mid-point of the desorption isotherm, are also list in Table 4. The values of the alloys annealed between 950–975 ˚C are similar, suggesting similar metal-hydrogen bond strength in the alloys due to their substantial A_2B_7-type main phase. Table 4 also lists the absorption and desorption equilibrium pressures at the mid-point, P_a and P_d, which are used to determine the hysteresis of the PCT isotherms, defined as ln (P_a/P_d). The hysteresis can be used to predict the pulverization rate of the alloy during cycling. In this case, hysteresis decreases with increasing mass of the Ce_2Ni_7-type phase by annealing and the hysteresis of the single-phase alloys are the lowest. According to the hysteresis data, a smaller degree of pulverization of the alloy particles and increasing in cycling stability are expected for the single-phase alloys.

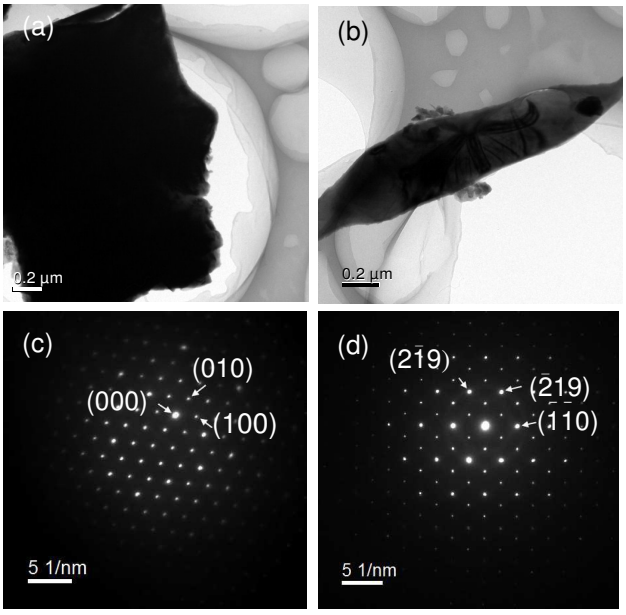

Fig. 4 TEM micrographs of the alloy annealed at 900 ˚C for Ce_2Ni_7-type grain in bright field mode (a), Cd_2Co_7-type grain in bright field mode (b), the selected-area electron diffraction (SAED) pattern taken along the zone axe of [001] of Ce_2Ni_7-type grain (c) and SAED pattern taken along the zone axe of [$\bar{3}$31] of Gd_2Co_7-type grain (d).

The enthalpy change (ΔH) and entropy change (ΔS) are used to estimate the heat of hydride reaction and the change in entropy, respectively. The calculated values based on the mid-point pressures for all annealed alloys are listed in Table 4. ΔS for the alloys are similar. However, for H_2 absorption, $-\Delta H$ increases slowly from 31.84 kJ mol^{-1} to 32.22 kJ mol^{-1} and decreases slightly to 32.18 kJ mol^{-1} with increasing annealing temperature, and it reaches to a maximum value for the alloy annealed 950 ˚C. The similar trend is also seen for H_2 desorption. The enthalpy change of the single-phase alloy indicates that hydrogen storage stability of the alloy is better than other alloys.

Fig. 5e shows the hydrogen absorption curves of the three kinds of annealed alloys at 298 K. It shows that the time to reach its 90% of the maximum hydrogen storage capacity for the single-phase alloy is 16.5 min, and that for the double-phase alloy with minor Cd_2Co_7-type phase is half of time of the single-phase

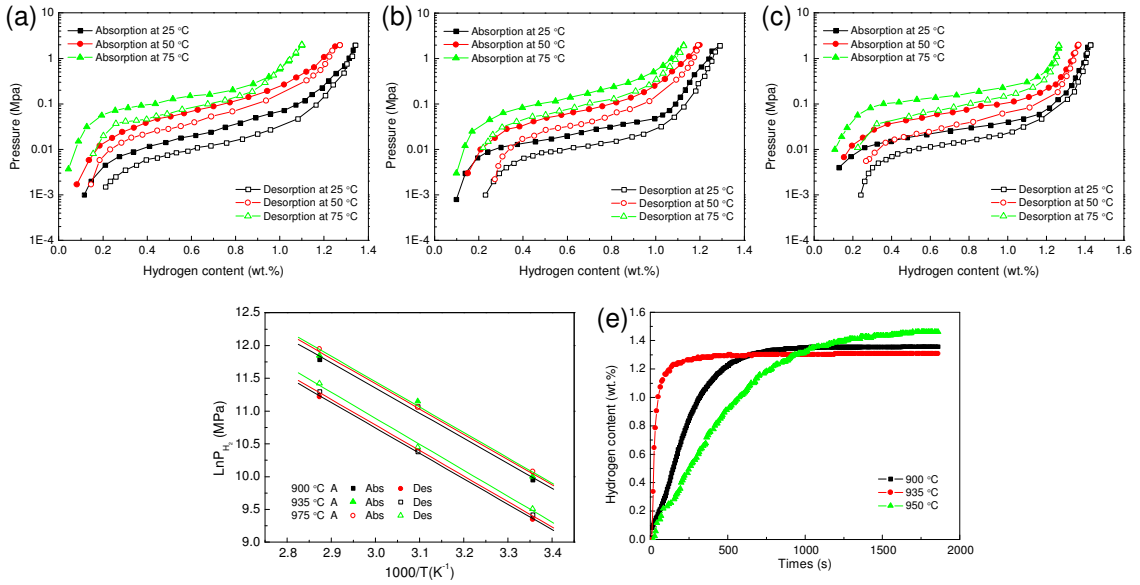

Fig. 5 PCT isotherms of the alloy annealed at 900 ˚C (a), 935 ˚C (b), 950 ˚C (c), Van't Hoff plots logP_{H2} vs. 1000/T (d) and hydrogen absorption curves (e) of the three alloys.

Table 4 Summary of gaseous hydrogen storage properties of the annealed alloys

Alloy	Max. H-storage @ 25 ˚C (wt. %)	Rev. H-storage @ 25 ˚C (wt. %)	Mid-point pressure @ 25 ˚C (Mpa)	Hysteresis @ 25 ˚C	10th H-storage @ 25 ˚C (wt. %)	$\triangle H$ (kJ mol^{-1} H_2)		$\triangle S$ (J K^{-1} mol^{-1} H_2)	
						Hydriding	Dehydriding	Hydriding	Dehydriding
895 ˚C	1.34	1.10	0.010	0.606	0.905	-31.80	32.21	-190.2	187.0
900 ˚C	1.34	1.11	0.012	0.602	0.915	-31.84	32.28	-189.9	186.1
925 ˚C	1.35	1.13	0.011	0.592	0.948	-31.90	32.31	-190.4	189.3
935 ˚C	1.29	1.06	0.012	0.581	0.939	-32.03	32.37	-191.0	186.8
945 ˚C	1.30	1.10	0.012	0.580	0.948	-32.11	32.42	-191.1	187.5
950 ˚C	1.43	1.19	0.014	0.578	1.050	-32.22	32.49	-191.5	189.4
975 ˚C	1.41	1.18	0.013	0.576	1.020	-32.18	32.40	-191.1	189.3

alloy. The alloy with minor Ce_5Co_{19}-type phase shows fast hydrogen absorption, which takes only, needs 2 min to reach 90%of its maximum hydrogen storage capacity. The results indicate that multiphase structure facilitates the hydrogen absorption kinetics of an alloy, especially with the Ce_5Co_{19}-type phase as the minor phase, which exhibits catalytic effect for hydrogen absorption.

The changes in the hydrogen storage capacity retention with cycle number of the alloys are shown in Fig. 6a. The hydrogen storage capacities of each annealed alloy after 10 cycles are also listed in Table 4. The hydrogen storage capacity retention of the single-phase alloy is the highest, and it also shows slower attenuation of the capacity retention. Fig. 6b,c is the SEM images of the annealed samples with different phase compositions after gas-solid hydrogenation/dehydrogenation cycling, which show the particle size of the single-phase alloy after cycle 10 times hydrogenation/dehydrogenation is much larger than that of the double-phase with Gd_2Co_7-type as the minor phase. The result indicates that the single-phase alloy exhibits a weaker pulverization and the appearance of minor phase leads to pulverization. The severe pulverization for multiphase alloys is related to the exacerbated lattice internal stress and lattice volume expansion when hydrogen atoms enter into the lattice, which leads to severe pulverization of the alloy.

3.3. Electrochemical measurement

Electrochemical properties of the as-cast and the annealed alloy electrodes are summarized in Table 5. All electrodes can be activated with 2 cycles (*N*), except for the alloys annealed between 935–945 ˚C. This can be attributed to the presence of minor Ce_5Co_{19}-type phase, which is more difficult to be activated than the A_2B_7-type phases. Young et al. reported that the alloy samples of the Ce_2Ni_7-type single phase that are annealed at higher temperatures are not more difficult to be activated.[8] The discrepancy we observed here may be due to the difference in elemental composition of the alloys used in this study.

Fig. 7 shows the relationship between discharge capacity and cycle number of the alloy electrodes. The results show the maximum discharge capacities of the alloys increase after annealing. The single-phase alloys exhibit excellent discharge capacities as high as 394 mAh g^{-1}, which is about 25% higher than the commercialized AB_5 alloys. The annealed alloys are

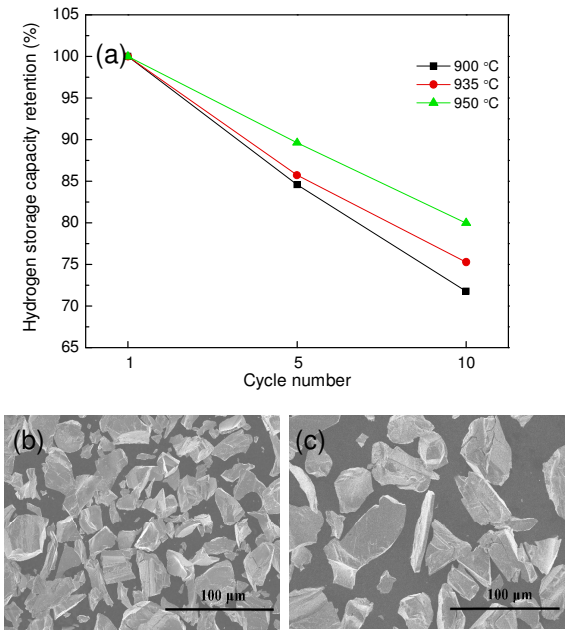

Fig. 6 Hydrogen storage capacity retention vs. cycle number of the alloys annealed at 900, 935 and 950 ˚C (a), and SEM micrographs with 10 hydrogenation/dehydrogenation cycles for the alloy annealed at 900 ˚C (b) and 950 ˚C (c).

classified into four groups based on their phase composition: 1) Ce_2Ni_7-type main phase with Gd_2Co_7-type and Ce_5Co_{19}-type (annealed at 890 ˚C) minor phases, 2) Ce_2Ni_7-type main phase with Gd_2Co_7-type minor phase (annealed at 900–925 ˚C), 3) Ce_2Ni_7-type main phase with Ce_5Co_{19}-type minor phase (annealed at 935–945 ˚C), and 4) Ce_2Ni_7-type single phase (annealed at 950–975 ˚C). The maximum discharge capacities of these four groups of alloys are in the order of Ce_2Ni_7-type (~394 mAh g^{-1}) > Ce_2Ni_7/Gd_2Co_7-type (~382 mAh g^{-1}) > Ce_2Ni_7/Ce_5Co_{19}-type (~377 mAh g^{-1}) > $Ce_2Ni_7/Gd_2Co_7/Ce_5Co_{19}$-type (~375 mAh g^{-1}), as shown in Fig. 7. This result indicates that the presence of a second phase deteriorates the discharge capacity property and the cycling stability of an alloy. Moreover, the discharge capacity of A_2B_7–type phase is higher than that of A_5B_{19}-type phase. The outstanding maximum discharge capacities of Ce_2Ni_7-type single-phase alloys are attributed to their compositional homogeneity after annealing, which is a result of decreasing lattice strain, finer grain size, and reducing lattice defect.[21] The theoretical discharge capacities for annealed alloys, based on the gaseous phase maximum hydrogen storage capacities, are also listed in Table 5. All samples show higher (about 20 mAh g^{-1}) full discharge capacities compared to their theoretical values. This excess capacity observed may be related to the incompletion of gaseous phase hydride formation in these samples with relatively tilted PCT isotherms, which may be activated electrochemically.[3,22]

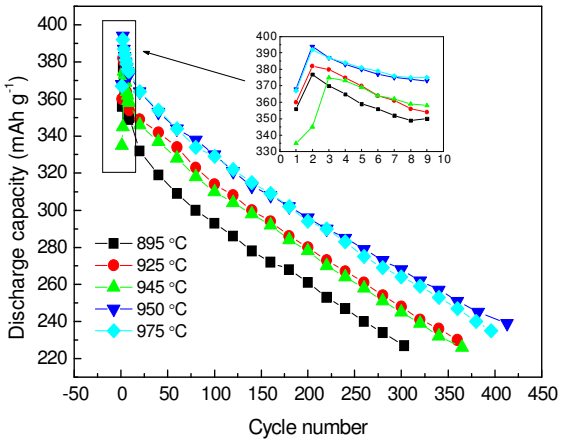

Fig. 7 Discharge capacity vs. cycle number of the annealed alloys measured in half-cell with $Ni(OH)_2$ as the positive electrode discharging at 72 mA g^{-1} until decreasing to 60% of the maximum discharge capacity value.

HRD reflects the discharge capability at large discharge current densities of the alloy electrodes and is evaluated by the ratio of discharge capacities measured at the discharge current density of 1440 mA g^{-1} to that measured at 72 mA g^{-1}. As shown in Table 5, the HRD decreases with reducing number of the phases of the alloys, which is directly proportional to the number of layers of the phase boundary among the alloys. The more boundaries in a alloy, the faster hydrogen can pass though, therefore, improving the HRD.[21] Among the two double phase alloys with Ce_2Ni_7-type as the main phase and Ce_5Co_{19}-type as the minor phase show improved HRD, compared to the alloys with Gd_2Co_7-type phase as the minor phase. This suggests the Ce_5Co_{19}-type phase may play a catalytic role as $LaNi_5$ phase due to its higher amount of Ni than A_2B_7–type phases, which provides a synergetic effect to the HRD performance. Conventionally, both the bulk diffusion coefficient (D) and surface exchange current (I_o) are used to study the change in HRD.[23] The details of both parameters are also listed in Table 5. The sample annealed at 890 ˚C has the highest D and I_o values, indicating easier hydrogen transportation in the bulk and faster charge transfer on the surface of the alloy. For the double-phase alloys, the D values are similar, but the I_o values of the alloys with the Ce_5Co_{19}-type minor phase

Table 5 Summary of electrochemical properties of the as-cast and annealed alloy electrodes

Alloys	N	Full Cap. @55 mAh g^{-1} (mAh g^{-1})	Theoretical Cap. based on PCT. @25 ˚C (mAh g^{-1})	S_{100} (%)	S_{200} (%)	Cycle achieved 60% cap.	*HRD* @ 1440 mA g^{-1} (%)	Diffusion coefficient D (10^{-10} cm^2 s^{-1})	Exchange current I_0 (mA g^{-1})
As-cast	2	325	-	64.6	51.7	142	44.3	1.45	46.5
895 ˚C	2	377	353	77.7	69.3	303	46.6	1.54	49.8
900 ˚C	2	379	354	78.1	71.0	325	39.0	1.34	43.9
925 ˚C	2	382	356	82.1	73.3	360	38.4	1.31	43.5
935 ˚C	3	374	340	82.4	74.1	363	42.5	1.36	45.2
945 ˚C	3	375	343	82.6	74.1	365	39.5	1.30	44.9
950 ˚C	2	394	378	83.7	74.4	413	37.3	1.23	40.3
975 ˚C	2	392	372	83.9	74.2	395	36.9	1.21	40.9

are larger than those of the alloys with the Gd_2Co_7-type minor phase. The I_o values of the single-phase alloys are smaller than other alloys, suggesting it is more difficult to activate the surface of a more homogenous alloy. In conclusion, the HRD characteristic is determined by both bulk and surface properties of an alloy and is closely related to its phase composition.

Fig. 7 also shows a comparison of the electrochemical cycling stability of the four groups of annealed samples, containing two single-phase alloys obtained at 950 and 975 ˚C. The single-phase alloy annealed at 950 ˚C can achieve 413 cycles, where the discharge capacity reduces to 60% of its maximum value. The capacity retentions at the 100th and 200th cycles (S_{100} and S_{200}) of the single-phase alloy are 83.7% and 74.4% (Table 5), respectively, which are much higher than those of the multiphase annealed alloys. Besides, as the annealing temperature increases, the capacity retention benefited from the gradual increasing abundance of the Ce_2Ni_7-type phase after annealing becomes more noticeable. The hysteresis from PCT supports the cases with higher annealing temperatures. We also observed a higher cycling stability for the single-phase alloy annealed at 950 ˚C compared to that annealed at 975 ˚C. This may be attributed to a more complete crystal structure and a finer grain for the single-phase alloy annealed at 950 ˚C, which is related to its lattice constants.

3.4. Cycling behavior study

SEM was performed on alloy samples with initial activation and activated samples with 10, 20, and 40 charge/discharge cycles to demonstrate the cycling stability for the alloys in terms of their phase composition. Fig. 8 shows the SEM images of the as-cast alloy (Fig. 8a_0–a_3) and the alloys annealed at 890 ˚C (Fig. 8b_0–b_3), 945 ˚C (Fig. 8c_0–c_3) and 950 ˚C (Fig. 8d_0–d_3). It is observed that oxidization and pulverization of the annealed alloys (Fig. 8b_0,c_0,d_0) after the initial activation are not apparent, while the oxidization of the as-cast alloy (Fig. 8a_0) is obvious. Oxidization and pulverization of the alloys also persist for the following cycles. As shown in Fig. 8a_2,b_2, many cracks are developed on the surface of the large particles of the alloys with four and three phases (as-cast and annealed at 890 ˚C alloys, respectively) after 20 cycles, and the plenty of white oxide of the surface indicates the oxidization-pulverization are in progress. Compared to the three- and four-phase alloys, the double- and single-phase alloys exhibit excellent pulverized resistance and antioxidant ability, as shown in Fig. 8c_0–c_3 and 8d_0–d_3. In addition, the particle size of the alloys annealed at 890, 945, and 950 ˚C after 100 cycles (Fig. S2) shows that the size of the single-phase alloy particles changed little, which decreases from 39.3 μm to 34.3 μm, while those of the multiphase alloys have pulverized extensively. To investigate the superior cycling stability observed for the single-phase alloy, the morphology and structure changes of the single-phase alloy annealed at 950 ˚C are analyzed by XPS, SEM, XRD and TEM. The surface characteristics of the single-phase alloy analyzed by XPS with 10, 20, 40, and 100 charge/discharge cycles are shown in Fig. 9. XPS analysis shows that the La3d (Fig. 9a) and Ni2p (Fig. 9c) peaks of the single-phase alloy are moving continuously

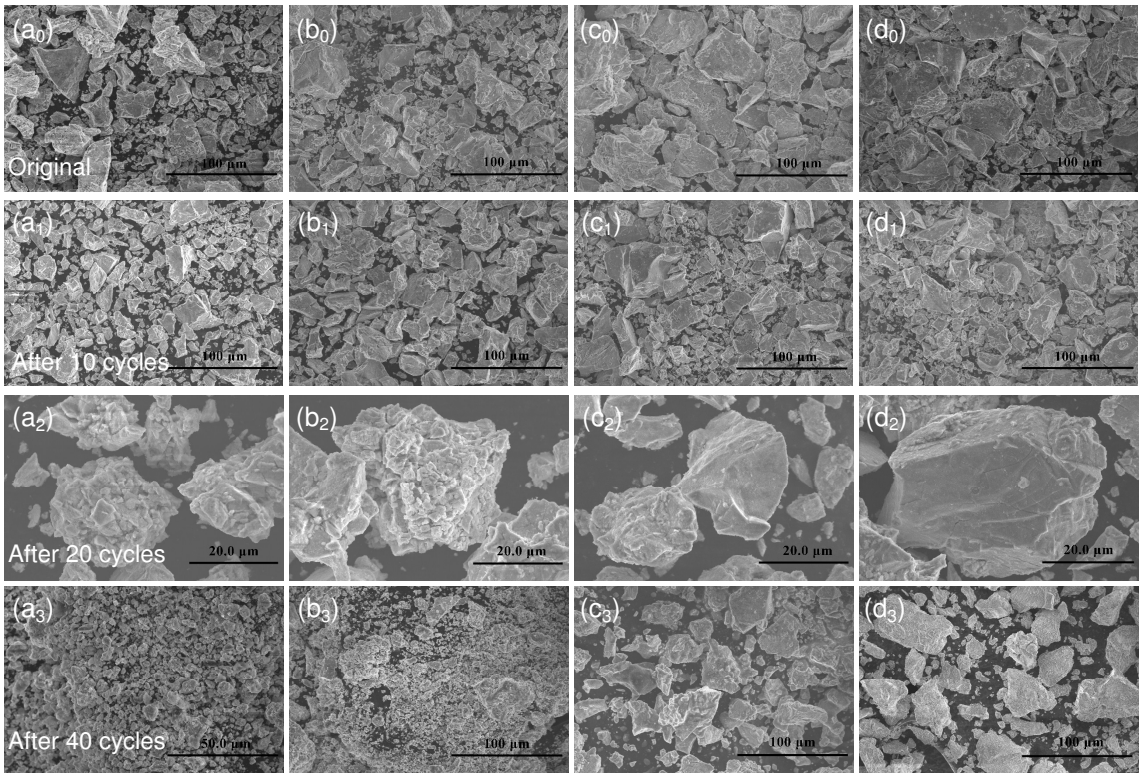

Fig. 8 SEM micrographs of the original alloy and alloys with 10, 20 and 40 charge-discharge cycles for the as-cast alloy (a_0-a_3), the alloy annealed at 890 ˚C (b_0-b_3), 945 ˚C (c_0-c_3) and 950 ˚C (d_0-d_3) (the horizontal direction is four groups of the alloys at a same cycling state and vertical direction is one alloy at various cycling states).

from lower binding energies to higher ones with cycling in the alkaline electrolyte, indicating that the active components on the alloy electrode surface are gradually oxidized. Fig. 9b shows that the Mg2p peak located at 49.9 eV is larger than that of metallic Mg (49.75 eV), indicating that Mg in the alloy has been oxidized to form MgO due to exposure of the alloy surface to air. After charge/discharge cycling, the binding energy for Mg2p decreases owing to the oxidization to $Mg(OH)_2$ (49.5 eV),[24] and its relative intensity almost disappears as the cycling number further increases, which may be attributed to the non-crystallization of the $Mg(OH)_2$ crystal with long cycling.

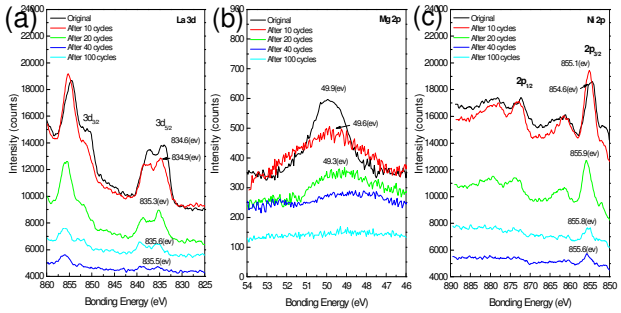

Fig. 9 XPS spectra of the alloy annealed at 950 ˚C for La3d (a), Mg2p (b) and Ni2p (c) of the original alloy and alloys with 10, 20, 40 and 100 charge-discharge cycles.

Fig. 10 shows the SEM images of the single-phase alloy annealed at 950 ˚C, showing the surface microstructure change with charge/discharge cycles. It is clear that the alloy surface exhibits very minor white nano-structured needles after 2 cycles (Fig. 10a) and the amount increases as cycling to 10 cycles (Fig. 10b). After cycling to 20 cycles, the surface is decorated with larger-scaled rods embraced in aggregation of small needles and the surface of the single-phase alloy is almost completely covered by the rods of ca. 1 μm in length (Fig. 10c). When cycling to 40 cycles, flaky material with a regular hexagon shape is observed (Fig. 10d). The regular flaky material distributes dispersedly among many irregular ones (Fig. 10e), and each alloy particle is wrapped with lamellar material when cycling to 100 cycles (Fig. 10f). Based on these results, it can be concluded that the material on the alloy surface are deemed to be hydroxides from the precipitation of rare earth ions (La^{+3} and Mg^{+2}) after oxidation by the electrolyte. In the early stages of oxidation of the alloy, the needles and rods on the surface are almost composed of precipitation of rare earth ions of La^{+3} as examined by X-ray energy dispersive spectroscopy (EDS) analysis, and Mg is absent in the rods and needles.

Fig. 11 shows the XRD patterns of single-phase alloy annealed at 950 ˚C after cycling 2–250 cycles. Although the double-phase and the single-phase alloys both show superior cycling stability, the crystal structure of the single-phase alloy preserves well after cycling 100 cycles (Fig. 11a), but the peak intensity decreases with cycle number from 100 to 250 cycles (Fig. 11b). As shown in Fig. S3, for the double-phase alloys, except for the clear peaks of hydroxide, the XRD peaks show distortion after cycling, and the peaks of the as-cast alloy almost disappears at 100 cycles. This result suggests that the lattice distortion in the single-phase phase has been reduced and the lattice strain can be weakened, attributed to the accordance in expansion/contraction during electrochemical hydrogen absorption/desorption. Therefore, the single-phase alloy has an extended cycle life comparing with multiphase alloys. As shown in Fig. 11a and Fig. S3, the (110) and (101) peaks of $La(OH)_3$ appear at 10 cycles and strengthen with increasing cycling, and the (211) peak of $La(OH)_3$ (48.65°) appears at 20 cycles. However, the (001) and (101) peaks of $Mg(OH)_2$ do not become noticeable until 40 cycles. Moreover, the relative peak intensity of the $Mg(OH)_2$ (101) peak is higher than that of the neighboring $La(OH)_3$ (201) peak only at 40 cycles but is lower at any other time. This suggests that the $Mg(OH)_2$ crystal form is relatively perfect than $La(OH)_3$. Therefore, combining with the SEM analysis, we can deduce that the nucleation rate of the surface hydroxide of La element is faster than that of Mg element. The growth of La hydroxide is from nano-structured needles to larger-scaled rods and to unformed hexagonal flake. The formation of Mg hydroxide is from both lamellar precipitation of Mg, resulted from Mg^{+2} reacting with the appropriate alkali solvent environment (40 cycles), and unformed hexagonal flake precipitation of $Mg(OH)_2$. Besides, as shown in Fig. 11d, except for peaks of the Ce_2Ni_7-type phase, $La(OH)_3$ and $Mg(OH)_2$ are observed, and small amount of $LaNi_5$ and Ni phase peaks can be detected after cycling 100 cycles, indicating that the phase decomposition of the single-phase alloy occurs.[17]

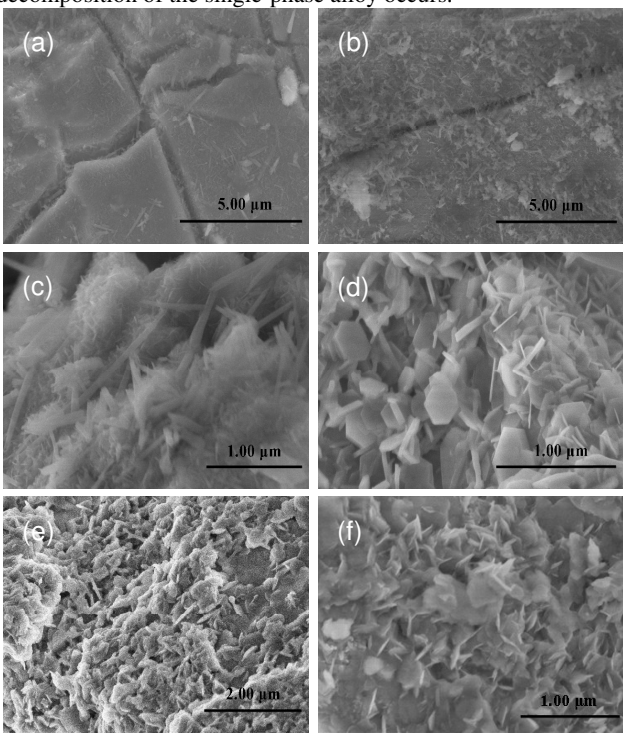

Fig. 10 Amplification SEM of the surface micrographs for the alloy annealed at 950 ˚C with 2 (a), 10 (b), 20 (c), 40 (d-e) and 100 (f) charge-discharge cycles.

In order to further investigate the cycling behavior of the single-phase alloy, TEM analysis is also performed and the results are shown in Fig. 12. Fig. 12a,e shows the morphology of

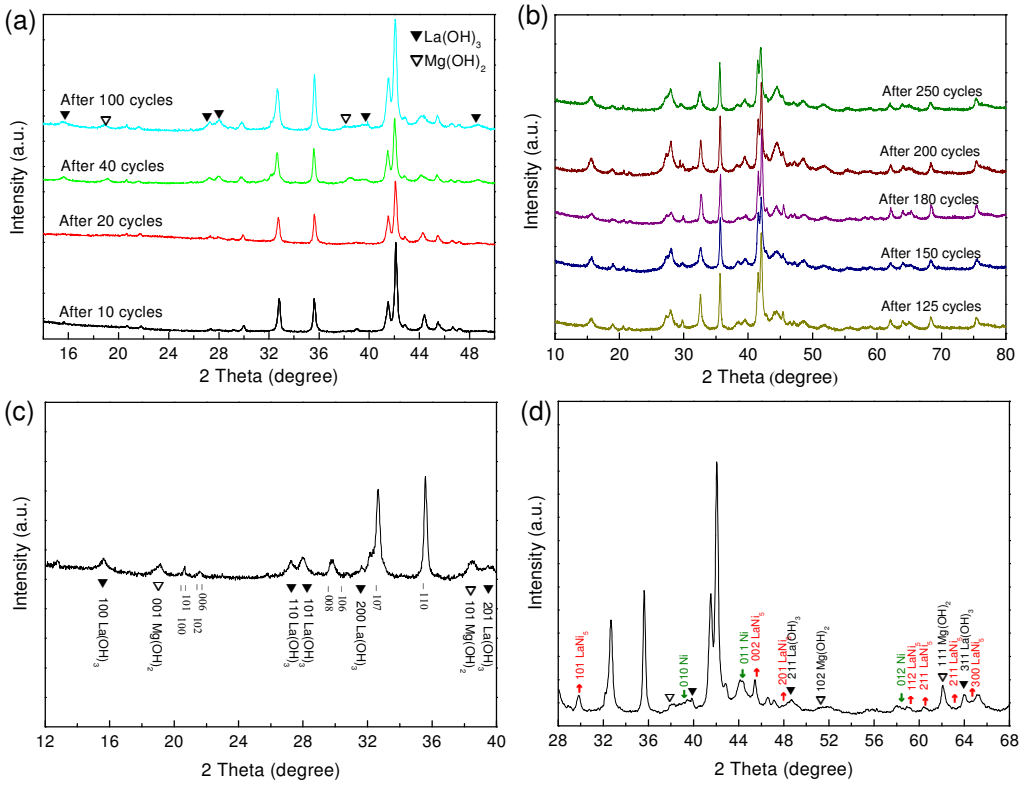

Fig. 11 XRD patterns of the alloy annealed at 950 ˚C after charge-discharge with 10–100 cycles in the 2θ range of 14–50° (a), 125–250 cycles in the 2θ range of 10–80° (b), 40 cycles in the 2θ range of 12–40° (c) and 100 cycles in the 2θ range of 28–68° (d). The diffraction peaks of $La(OH)_3$ (solid triangle; PDF n°00-036-1481) and of $Mg(OH)_2$ (hollow triangle; PDF n°00-007-0239) are shown beside the peaks of the Ce_2Ni_7-type phase (vertical bars) in (c), and the diffraction peaks of $LaNi_5$ (up arrow; PDF n°00-065-1107) and Ni (down arrow; PDF n°00-065-2865) are shown as red and green colors, respectively.

the alloy after cycling 100 cycles for crystal particles α and β, in which the uniform alloy body and body wrapped with foggy aggregated materials are recorded, respectively. Fig. 12c,d is the bright field and dark field TEM micrographs from a typical boundary between the surface layer and the metal alloy can be clearly seen in these two micrographs, and the surface layer is filled with many bright embedded nano-sized inclusions. The corresponding SAED patterns of the alloy surface layer and the alloy body are shown in Fig. 12b. The pattern of the halos in the Fig. 12b suggests two types of interlayer spacing distances of 0.319 (inner) and 0.206 nm (outer), which are very close to the inter-planar distances of $La(OH)_3$ (101) with hexagonal structure (space group P63/m) and Ni (111) with cubic structure (space group Fm-3m), respectively (see supplementary information Table S1). Therefore, we can conclude that the inclusions in thesurface layer are nanocrystal Ni. The SAED pattern of β consists of two features, including spotty rings and halos, as shown in Fig. 12f. The spotty rings in lines in the image are the metal alloy, in which the lines associate to lattice strain caused by lattice distortion of the metal alloy, and the halos are identified as $LaNi_5$ (space group P6/mmm) structure with crystal indices of (101) for the inner ring and of (213) for the outer ring (Table S1). The result indicates that some of the Ce_2Ni_7-type single-phase structure has decomposed to $LaNi_5$ structure after cycling.[17]

Based on the above analyses, we can conclude that the electrochemical discharge capacity degradation with cycling of the Ce_2Ni_7-type single-phase alloy are mainly due to the oxidation of La and Mg. The oxidization of La occurs prior to that of Mg. $La(OH)_3$ grows from nano-structured needles to larger-scaled rods then to unformed lamellar hydroxide, while Mg precipitates into irregular lamellar shape embraced with hexagonal flakes. Furthermore, the crystal structure of the single-phase alloy can preserve well within 100 charge/discharge cycles, but $LaNi_5$ and nanocrystal Ni inclusions are found in the body and the surface oxide layer of some crystal particles, respectively, after a long time cycling. Pulverization is more severe for main/minor phase structured alloys but it is not as apparent for single-phase structured alloys.

4. Conclusion

The phase transformation and cycling characteristic of the Ce_2Ni_7-type single-phase $La_{0.78}Mg_{0.22}Ni_{3.45}$ alloy were studied in this paper. The Ce_2Ni_7-type single-phase $La_{0.78}Mg_{0.22}Ni_{3.45}$ alloy is obtained by zoning annealing treatment method. The non-super-stacking $CaCu_5$- and $MgCu_4Sn$-type phases transform to super-stacking phases under 890 ˚C. The Ce_5Co_{19}-type phase transforms to the Ce_2Ni_7-type phase via a peritectic reaction at a temperature range of 890–900 ˚C. The Gd_2Co_7-type phase melted and decomposed to the Ce_5Co_{19}-type phase, and the newly form-

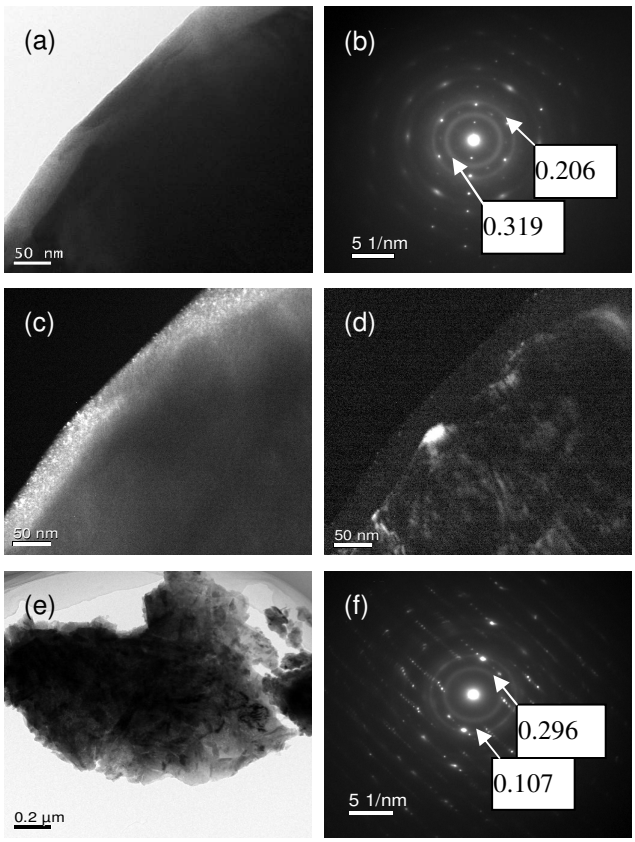

Fig. 12 TEM micrographs of the alloy annealed at 950 ˚C with 100 charge-discharge cycles for the crystal particle α of the morphology image (a), SAED pattern (b), bright field mode (c), dark field mode (d) and for crystal particle β of morphology image (e), SAED pattern for boundary (f).

ed Ce_5Co_{19}-type phase reacts to the Ce_2Ni_7-type phase to form an alloy with Ce_2Ni_7/Gd_2Co_7 structure during 900–925 ˚C. During 925–935 ˚C, the Gd_2Co_7-type phase totally converts to the Ce_5Co_{19}-type phase, and the alloys are composed of Ce_2Ni_7/Ce_5Co_{19} structure within 935–945 ˚C. The minor Ce_5Co_{19}-type phase finally transforms to the Ce_2Ni_7-type single phase at the temperature range of 945–950 ˚C, and the Ce_2Ni_7-type single phase is stable in the temperature of 950–975 ˚C. The single-phase Ce_2Ni_7-type $La_{0.78}Mg_{0.22}Ni_{3.45}$ alloy exhibits high gaseous phase hydrogen storage and electrochemical capacities, low PCT hysteresis and enthalpy change ΔH for hydrogenation, as well as outstanding cyclic stability. The capacity attenuation of the Ce_2Ni_7-type single-phase alloy is mainly due to the loss of active material resulted from oxidization of La and Mg to hydroxides. Oxidization of La is earlier than that of Mg. The precipitation of La is accompanied by its growth from nano-structured needles to larger-scaled rods and to irregular hexagonal flakes, but Mg precipitates to regular and unformed lamellar $Mg(OH)_2$. Pulverization of the single-phase alloy is not severe. Within 100 charge-discharge cycles, the crystal structure of the Ce_2Ni_7-type single-phase alloy remains well and the reduction in particle size is not apparent. Whereas for the Ce_2Ni_7-type multiphase alloys, distortion of their crystal structure appears at early cycles and large reduction of their particle size is observed.

Acknowledgment

This work (research) was financially supported by the National Natural Science Foundation of China (NOs. 51171165 and 21303157), the Natural Science Foundation of Hebei Province (NOs. B2012203027 and B2012203104), and the China Postdoctoral Science Foundation Project (2013M541201).

Notes and References

[a] *State Key Laboratory of Metastable Materials Science and Technology, Yanshan University, Qinhuangdao 066004, PR China*
[b] *Hebei Key Laboratory of Applied Chemistry, School of Environmental and Chemical Engineering, Yanshan University, Qinhuangdao 066004, PR China*
[c] *Baotou Research Institute of Rare Earth, Baotou 014030, PR China*
Tel & fax: +86-335-8074648. E-mail address: hanshm@ysu.edu.cn.

† Electronic Supplementary Information (ESI) available: [details of any supplementary information available should be included here]. See DOI: 10.1039/b000000x/

1 Y.F. Liu, H.G. Pan, M.X. Gao, and Q.D. Wang, *J Mater Chem*, 2011, **21**, 4743.
2 C.C. Nwakwuo, T. Holm, R.V. Denys, W.K. Hu, J.P. Maehlen, J.K. Solberg, and V.A. Yartys, *J Alloys Compd*, 2013, **555**, 201.
3 K. Young, D.F. Wong, L. Wang, J. Nei, T. Ouchi, and S. Yasuoka, *J Power Sources*, 2015, **277**, 426.
4 T. Kohno, H. Yoshida, F. Kawashima, T. Inaba, I. Sakai, M. Yamamoto, and M. Kanda, *J Alloys Compd*, 2000, **311**, L5.
5 J.J. Liu, S.M. Han, Y. Li, S.Q. Yang, W.Z. Shen, L. Zhang, and Y. Zhou, *J Alloys Compd*, 2013, **552**, 119.
6 Y.F. Liu, H.G. Pan, M.X. Gao, Y.Q. Lei, and Q.D. Wang, *J Electrochem Soc*, 2005, **152**, A1089.
7 Y.F. Liu, H.G. Pan, Y.J. Yue, X.F. Wu, N. Chen, and Y.Q. Lei, *J Alloys Compd*, 2005, **395**, 291.
8 K. Young, T. Ouchi, and B. Huang, *J Power Sources*, 2014, **248**, 147.
9 W.K. Hu, R.V. Denys, C.C. Nwakwuo, T. Holm, J.P. Maehlen, J.K. Solberg, and V.A. Yartys, *Electrochim Acta*, 2013, **96**, 27.
10 J.J. Liu, S.M. Han, Y. Li, J.L. Zhang, Y.M. Zhao, and L. Che, *Int J Hydrogen Energy*, 2013, **38**, 14903.
11 Y.F. Liu, Y.H. Cao, L. Huang, M.X. Gao, and H.G. Pan, *J Alloys Compd*, 2011, **509**, 675.
12 J. Monnier, H. Chen, S. Joiret, J. Bourgon, and M. Latroche, *J Power Sources*, 2014, **266**, 162.
13 L. Zhang, J.L. Zhang, S.M. Han, Y. Li, S.Q. Yang, and J.J. Liu, *Intermetallics*, 2015, **58**, 65.
14 R.V. Denys, B. Riabov, V.A. Yartys, R.G. Delaplane, and M. Sato, *J Alloys Compd*, 2007, **446–447**, 166.
15 R.V. Denys, A.B. Riabov, V.A. Yartys, M. Sato, and R.G. Delaplane, *J Solid State Chem*, 2008, **181**, 812.
16 M.N. Guzik, B.C. Hauback, and K. Yvon, *J Solid State Chem*, 2012, **186**, 9.
17 L. Zhang, S.M. Han, D. Han, Y. Li, X. Zhao, and J.J. Liu, *J Power Sources*, 2014, **268**, 575.
18 X.B. Zhang, D.Z. Sun, W.Y. Yin, Y.J. Chai, and M.S. Zhao, *J Power Sources*, 2006, **154**, 290.
19 Z. Deyuan, J. Tang, and K.A. Gschneidner Jr, *J Less-Comm Met*, 1991, **169**, 45.
20 M. Huang, R.W. McCallum, and T.A. Lograsso, *J Alloys Compd*, 2005, **398**, 127.
21 S. Srivastava, and O.N. Srivastava, *J Alloys Compd*, 1999, **282**, 197.
22 K. Young, T. Ouchi, and B. Huang, *J Power Sources*, 2012, **215**, 152.
23 H.G. Pan, J.X. Ma, C.S. Wang, S.A. Chen, X.H. Wang, C.P. Chen, and Q.D. Wang, *J Alloys Compd*, 1999, **293–295**, 648.
24 Y.F. Liu, H.G. Pan, M.X. Gao, H. Miao, Y. Lei, and Q. Wang, *Int J Hydrogen Energy*, 2008, **33**, 124.